


Depth- and curvature-based quantitative susceptibility mapping analyses of cortical iron in Alzheimer's disease

Jenna L. Merenstein ^{1,*}, Jiayi Zhao¹, Devon K. Overson^{1,2}, Trong-Kha Truong^{1,2}, Kim G. Johnson³, Allen W. Song^{1,2}, David J. Madden^{1,3,4}

¹Brain Imaging and Analysis Center, Duke University Medical Center, Durham, NC 27710, United States,

²Medical Physics Graduate Program, Duke University, Durham, NC 27708, United States,

³Department of Psychiatry and Behavioral Sciences, Duke University Medical Center, Durham, NC 27710, United States,

⁴Center for Cognitive Neuroscience, Duke University, Durham, NC 27708, United States

*Corresponding author: Brain Imaging and Analysis Center, Duke University Medical Center, Box 3918, Durham, NC 27710, United States.

Email: jenna.merenstein@duke.edu

In addition to amyloid beta plaques and neurofibrillary tangles, Alzheimer's disease (AD) has been associated with elevated iron in deep gray matter nuclei using quantitative susceptibility mapping (QSM). However, only a few studies have examined cortical iron, using more macroscopic approaches that cannot assess layer-specific differences. Here, we conducted column-based QSM analyses to assess whether AD-related increases in cortical iron vary in relation to layer-specific differences in the type and density of neurons. We obtained global and regional measures of positive (iron) and negative (myelin, protein aggregation) susceptibility from 22 adults with AD and 22 demographically matched healthy controls. Depth-wise analyses indicated that global susceptibility increased from the pial surface to the gray/white matter boundary, with a larger slope for positive susceptibility in the left hemisphere for adults with AD than controls. Curvature-based analyses indicated larger global susceptibility for adults with AD versus controls; the right hemisphere versus left; and gyri versus sulci. Region-of-interest analyses identified similar depth- and curvature-specific group differences, especially for temporo-parietal regions. Finding that iron accumulates in a topographically heterogeneous manner across the cortical mantle may help explain the profound cognitive deterioration that differentiates AD from the slowing of general motor processes in healthy aging.

Key words: cortical columns; magnetic resonance imaging; neurodegeneration; spatial specificity; susceptibility-weighted imaging.

Introduction

Alzheimer's disease (AD) is an age-related neurodegenerative disorder characterized by the accumulation of amyloid beta ($A\beta$) plaques and tau neurofibrillary tangles in the brain (Braak and Braak 1991; Jack et al. 2018), which results in the progressive deterioration of cognitive abilities (Förstl and Kurz 1999). In addition to $A\beta$ and tau accumulation, AD is accompanied by elevated cerebral non-heme iron (Zecca et al. 2004; Long et al. 2023). Non-heme iron is the most abundant metal in the brain and is necessary for many essential neurobiological processes, including myelination and adenosine triphosphate synthesis in mitochondria (Zecca et al. 2004; Ward et al. 2014; Daugherty and Raz 2015). However, excessive non-heme iron accumulation disrupts homeostasis, leading to oxidative stress and ultimately neurodegeneration (Zecca et al. 2004; Ward et al. 2014).

Iron has magnetic properties that can be assessed in vivo using T2*-weighted structural magnetic resonance imaging (MRI) sequences enhanced with susceptibility-weighted angiography (SWAN), known as quantitative susceptibility mapping (QSM) (Haacke et al. 2005; Liu et al. 2015; Duyn and Schenck 2017; Yan et al. 2018; Ruetten et al. 2019). These sequences provide measures of positive (paramagnetic) susceptibility that are primarily sensitive to iron and measures of negative (diamagnetic) susceptibility that are sensitive to multiple neural substrates, including the degree of myelination (Liu et al. 2015; Deh et al. 2018; Shin et al. 2021) and potentially $A\beta$ aggregation (Gong et al. 2019). Several QSM studies of AD report elevated levels of iron

in deep gray matter (GM) nuclei (e.g. globus pallidus, caudate, putamen) when compared to healthy controls (Zhu et al. 2009; Acosta-Cabrero et al. 2013; Lei et al. 2018; Kuchcinski et al. 2023), but few studies have examined AD-related variation in susceptibility within the GM of the cortex.

Although the cortex accumulates relatively little iron in healthy adults across the lifespan (Hallgren and Sourander 1958; Acosta-Cabrero et al. 2016; Madden and Merenstein 2023), both ex vivo (Grundke-Iqbal et al. 1990; Smith et al. 1997; Lovell et al. 1998; Duce et al. 2010) and in vivo (van Bergen et al. 2016; Spotorno et al. 2020; Zhao et al. 2021; Sacchi et al. 2023) studies suggest that iron increasingly accumulates in cortical regions as they accumulate $A\beta$ and tau neuropathologies (Cogswell and Fan 2023). For example, $A\beta$ accumulates in densely connected hub regions (Dai et al. 2014; Bertolero et al. 2018; Clarke et al. 2022), including the posterior parietal cortex, cingulate gyrus, and insula, which also exhibit higher susceptibility in adults with AD relative to healthy controls (Zhu et al. 2009; Acosta-Cabrero et al. 2013; Kim et al. 2017; Yang et al. 2022). AD-related increases in susceptibility have also been observed within the temporal lobe (Kim et al. 2017; Bulk et al. 2018; Yang et al. 2022; Sacchi et al. 2023), which is the first region to accumulate tau (Braak and Braak 1991). In healthy adults, susceptibility in the inferior temporal cortex has even been shown to statistically mediate age-related decline in fluid cognition (Howard et al. 2022). However, prior studies conducted either whole-brain voxelwise analyses or averaged susceptibility across entire regions-of-interest (ROIs), and both approaches lack the spatial specificity

Received: September 20, 2023. Revised: November 21, 2023. Accepted: December 15, 2023

© The Author(s) 2024. Published by Oxford University Press. All rights reserved. For permissions, please e-mail: journals.permissions@oup.com

required to disentangle potential layer-specific differences in cortical susceptibility.

Examining susceptibility in a layer-specific manner is important because each cortical layer exhibits a distinct cytoarchitectural pattern in the type (e.g. granular versus pyramidal cells) and density of neurons, with three to four layers in the allocortex and six layers in the neocortex (Vogt and Vogt 1903). As a result, each cortical layer may differentially accumulate iron, especially in the context of neurodegeneration. However, ROI-based studies cannot resolve whether a significant difference in iron accumulation in AD relative to healthy controls is driven by elevated iron in superficial (i.e. higher layers toward the skull) versus deeper (i.e. lower layers toward white matter [WM]) cortical layers because they use values from an entire ROI. Voxelwise approaches can identify smaller clusters of significant differences in susceptibility, but the requirements for group-level registration and spatial smoothing still diminish the ability to isolate the location of a cluster on the cortical mantle.

We addressed these limitations here by conducting cortical column-based analyses of susceptibility for each individual participant. The term *column* as used in this context refers to the straight lines orthogonal to the cortical surface that connect the pial surface to the GM/WM tissue boundary. This definition of the term *column* differs conceptually from the definition used by *ex vivo* neuroanatomical studies, where cytoarchitecture is considered (Brodmann 1909). From these cortical columns, one can sample susceptibility along the various distances, or depths, from the pial surface through the cortical depths leading to the GM/WM boundary. One previous depth-wise study of healthy adults reported that susceptibility peaks at the GM/WM boundary of the middle frontal and precentral cortices (Lee et al. 2023). Another study extended these analyses to healthy younger and older adults and observed age-related differences across all depths of the primary motor cortex, although the largest age-related difference in susceptibility was associated with the superficial depths (Northall et al. 2023). In AD, differences in susceptibility may also be most apparent at superficial depths as these exhibit higher concentrations of $A\beta$ than deeper depths, at least in the temporal cortex (Kraszpulski et al. 2001).

Decreases in the degree of gyrification and increases in sulcal width may also contribute to differences in susceptibility in AD (Liu et al. 2012). The equivolume principle refers to the observation that the thickness of cortical layers differs as a function of curvature, such that the innermost layers of a curve are thicker and the outermost layers are thinner (Bok 1929; Waehnert et al. 2014; Consolini et al. 2022). As a result, superficial layers are thicker in sulci and thinner in gyri, whereas deeper layers are thicker in gyri and thinner in sulci. Relative to gyri, the sulci exhibit more pronounced atrophy (Im et al. 2008; Liu et al. 2013; Hamelin et al. 2015; Plochanski and Østergaard 2016) and $A\beta$ accumulation (Clinton et al. 1993) in AD. Examining susceptibility in cortical columns according to their curvature bin (i.e. gyral crown, sulcal bank, or sulcal fundus) may therefore provide additional anatomical specificity about the distribution of iron in AD.

The current study used a column-based approach to examine susceptibility across the entire cortical mantle at three levels of anatomical specificity: global cortical depth, global cortical curvature, and regional depth and curvature. We recruited 22 participants who were diagnosed with AD based on a biomarker framework (Jack et al. 2018) and 22 age- and sex-matched healthy controls. We focused our main analyses on group differences in positive susceptibility as it is widely accepted that iron is its primary neurobiological substrate (Haacke et al. 2005; Liu et al. 2015;

Ruetten et al. 2019). However, for completeness, we also report exploratory analyses of negative susceptibility, although its neurobiological underpinnings are still under debate (Duyn and Schenck 2017; Gong et al. 2019; Lazari and Lipp 2021; Zhao et al. 2021).

For the global depth-wise and curvature-based analyses, we hypothesized that positive and negative susceptibility values would both be significantly larger in participants with AD than healthy controls. For the ROI-based analyses, we hypothesized that group differences in susceptibility would be present in highly connected hub regions and temporal regions that are affected by $A\beta$ and tau, similar to prior work (Zhu et al. 2009; Acosta-Cabrero et al. 2013; Kim et al. 2017; Yang et al. 2022). Extending earlier work, however, we predicted that the significant group differences within these ROIs would be most pronounced for superficial cortical depths (Kraszpulski et al. 2001) and sulci (Clinton et al. 1993; Im et al. 2008; Liu et al. 2013; Hamelin et al. 2015; Plochanski and Østergaard 2016). All predicted group differences should be more apparent in the left than right hemisphere, as the left hemisphere exhibits more cortical iron (Yang et al. 2022), cortical thinning (Roe et al. 2021), and metabolic dysfunction (Loewenstein et al. 1989) in AD. By increasing the anatomical specificity and providing a more detailed perspective than can typically be obtained *in vivo*, the current methodology may identify more subtle patterns of iron accumulation in AD that may have been missed by earlier research.

Materials and methods

Participants

This study was conducted in compliance with the Code of Ethics of the World Medical Association (Declaration of Helsinki) for experiments involving humans and with the Institutional Review Board for Duke University Medical Center. All participants (and their caregivers, if necessary) provided written informed consent, were free of MRI contraindications (i.e. ferrous metal devices and implants), and were compensated for their time.

Participation in this study involved the completion of a 1-h. MRI scan, the Montreal Cognitive Assessment (Nasreddine et al. 2005), and a brief demographic questionnaire. A total of 22 participants diagnosed with AD were recruited from the Duke University–University of North Carolina (UNC) at Chapel Hill Alzheimer’s Disease Research Center (ADRC). Participants were diagnosed as having AD based on a multidisciplinary clinical consensus panel comprised of neurologists, psychiatrists, neuropsychologists, and research coordinators using the A/T/(N) criteria, as indicated previously (Jack et al. 2018). The panel takes into account patient and caregiver report of cognitive symptoms and functioning from the Clinical Dementia Rating (Morris 1993), Functional Activities Questionnaire (Pfeffer et al. 1982), and Neuropsychiatric Inventory (Cummings et al. 1994); neuropsychological testing measures from the Uniform Data Set 3 (Besser et al. 2018); and the degree of brain atrophy assessed by T1-weighted anatomical MRIs. We also assessed $A\beta$ status for 15 of the 22 participants with AD using cerebrospinal fluid ($n=14$) measures from a Fujirebio immunoassay (Fujirebio, Ghent, Belgium) or positron emission tomography ($n=1$) and confirmed $A\beta$ positivity for 13 out of 15 (87%) participants who had these measures available.

In addition, 22 cognitively healthy age- and sex-matched controls were recruited from the Duke–UNC ADRC ($n=10$) or an in-house dataset of high-functioning, community-dwelling volunteers ($n=12$). Control participants recruited from the Alzheimer’s Disease Research Center were deemed as having

Table 1. Participant characteristics.

Variable	Alzheimer's disease	Controls	t/ χ^2	P-value
n	22	22	ND	ND
Age				
Mean (SD)	67.30 (8.1)	67.10 (8.2)	0.075	0.941
Median (range)	68 (51–78)	68 (51–80)	ND	ND
Sex				
% Female	14 (63.6%)	14 (63.6%)	0.000	1.000
Education (years)				
Mean (SD)	16.0 (3.0)	17.1 (2.0)	1.467	0.150
Median (range)	16.0 (12–20)	18.0 (12–20)	ND	ND
Not reported	1 (4.5%)	0 (0%)	ND	ND
Montreal Cognitive Assessment				
Mean (SD)	16.9 (5.8)	28.2 (1.4)	8.981	<0.001
Median (range)	18.5 (4–25)	29.0 (25–30)	ND	ND
Race				
White	16 (72.7%)	20 (90.5%)	1.717	0.191
Black	5 (22.7%)	2 (9.5%)	ND	ND
Not reported	1 (4.5%)	0 (0%)	ND	ND
Handedness				
Right	20 (91%)	19 (86%)	0.002	0.961
Left	2 (9%)	2 (9.5%)	ND	ND
Not reported	0 (0%)	1 (4.5%)	ND	ND

Note. Continuous variables are presented with their corresponding mean (standard deviation, SD) and median (range), with group differences assessed using two-sample sample t-tests. Categorical variables are presented as n (%), with group differences assessed using chi-square (χ^2) tests. Significant group differences ($P < 0.05$; bolded) were only observed for the score on the Montreal Cognitive Assessment.

normal cognition using the criteria previously described for the participants diagnosed with AD. The community-dwelling volunteers did not receive formal clinical assessments but were required to have intact general cognition (score ≥ 25) on the Montreal Cognitive Assessment (Nasreddine et al. 2005), a score > 50 th percentile on the Wechsler Adult Intelligence Scale-III vocabulary subtest (Wechsler 1997), a score < 15 on the Beck Depression Inventory (Beck 1978), and normal (corrected) visual acuity (Snellen score $\geq 20/40$) on the Freiburg Visual Acuity Test (Bach 1996). The volunteers were also free of major neurological (e.g. epilepsy, stroke, psychosis) and medical (e.g. emphysema, uncontrolled hypertension) conditions, and were not taking medications known to affect cognitive function (e.g. antidepressants, antianxiolytics). Participant characteristics are provided separately for each group in Table 1.

Imaging data acquisition

All imaging data were acquired at Duke University Medical Center on a 3 T General Electric Signa Premier Ultra High Performance whole-body 60 cm bore MRI scanner (GE Healthcare, Waukesha, WI, USA) equipped with a 48-channel receive-only head coil. Participants wore earplugs to reduce scanner noise, and foam pads were used to minimize head motion. For each participant, we acquired a high-resolution anatomical image volume using a T1-weighted magnetization prepared rapid acquisition gradient echo sequence, a T2-weighted fluid attenuated inversion recovery (FLAIR) image volume, and a SWAN image volume using a multi-echo gradient recalled echo (GRE) sequence. There were some variations in the imaging acquisition parameters for each sequence, because data collection occurred over a period of 3 yr and included a combination of participants from two separate protocols. Importantly, however, the distribution of the sequences did not significantly differ between adults with AD and controls, $\chi^2 = 2.562$, $P = 0.278$ (Table 2).

During scanning, we also acquired resting-state functional MRI data, whole-brain human connectome project diffusion-weighted

imaging data, and high-resolution multi-shot multiplexed sensitivity encoding diffusion-weighted imaging data, to be reported separately.

Structural image preprocessing

The T1-weighted anatomical and T2-weighted FLAIR image volumes were first bias-corrected using the *N4BiasFieldCorrection* command from Advanced Normalization Tools (Avants et al. 2011). The bias-corrected T1-weighted image volumes were then used as input to FreeSurfer (Fischl et al. 1999) to (i) obtain meshes of the pial surface and the GM/WM boundary surface and (ii) estimate the cortical thickness and cortical curvature at each vertex. Next, the bias-corrected FLAIR image volume was registered to the T1-weighted image volume using the FreeSurfer *bbregister* command with six degrees of freedom. The bias-corrected FLAIR image volumes, in T1-weighted anatomical space, were also used in the FreeSurfer reconstruction process to more accurately estimate the pial surface (see <https://surfer.nmr.mgh.harvard.edu/fswiki/FreeSurferWiki>).

Estimation of quantitative susceptibility

We obtained susceptibility maps from the SWAN data using the Susceptibility Tensor Imaging Suite Version 3.0 (<https://people.eecs.berkeley.edu/~chunlei.liu/software.html>) in MATLAB (version 2017a). We performed Laplacian-based unwrapping of the phase images, removed the background field, and obtained a binary brain mask from the average magnitude image using FSL's brain extraction tool with a fractional intensity threshold of 0.6 (Jenkinson et al. 2002; Smith et al. 2004). Using the unwrapped phase images and the binary brain mask as inputs, susceptibility values were calculated using the iterative sparse linear equation and least-squares solver method (Li et al. 2011; Li et al. 2014). Susceptibility values were estimated directly without reference to any selected structure. Due to the presence of extreme oscillatory

Table 2. Imaging acquisition parameters.

TE	TR	Flip angle	Matrix size	Voxel size	Slices	SENSE	n AD	n Con.
T1-weighted magnetization prepared rapid acquisition gradient echo								
3.04	2076.99	8°	256 × 256 mm	1 × 1 × 1 mm	124	2	6	11
3.20	2100.23	8°	256 × 256 mm	1 × 1 × 1 mm	116	2	6	5
3.20	2132.80	8°	256 × 256 mm	1 × 1 × 1 mm	124	2	10	6
Susceptibility-weighted angiography								
24.31	39.60	15°	256 × 256 mm	1 × 1 × 1 mm	124	2	6	11
24.73	40.20	15°	256 × 256 mm	1 × 1 × 0.5 mm	232	2	6	5
24.73	40.20	15°	256 × 256 mm	1 × 1 × 1 mm	124	2	10	6
Fluid attenuated inversion recovery								
104.70	6302.00	90°	256 × 243 mm	0.5 × 0.5 × 0.7 mm	232	1	6	11
102.60	6302.00	90°	256 × 243 mm	0.5 × 0.5 × 0.7 mm	232	1	6	5
103.80	6302.00	90°	256 × 243 mm	0.5 × 0.5 × 0.7 mm	232	1	10	6

Note. TE = echo time (milliseconds); TR = repetition time (milliseconds); SENSE = sensitivity encoding factor; n = number of control participants (Con.) with the corresponding parameters; n = number of participants with AD for the corresponding parameters.

susceptibility values around the edges of the brain, the skull-stripped susceptibility map for each participant was eroded by a 1 mm³ spherical kernel using *fslmaths* to ensure more robust and reliable estimates in cortical regions located near the skull. For each participant, a trained researcher visually inspected the quality of the brain extraction and the degree of erosion to confirm that neither step was too liberal or too conservative. We further validated the suitability of this erosion step by quantifying that, on average, <5% of voxels from superficial depths were removed for any region-of-interest. The left frontal pole (5%) and left temporal pole (4%) were the regions most affected by this step, as expected from their proximity to the edge of the brain, and results from these regions should be interpreted with caution.

Cortical column construction

The pipeline for constructing cortical columns (Fig. 1) is a modification of a locally developed pipeline for cortical column-based analyses of diffusion-weighted imaging data in healthy younger adults (Ma et al. 2023). We generated cortical columns in each participant's native T1-weighted anatomical space, separately for each hemisphere, using the *write_mrtrix_tracks* command in MATLAB (version 2022a) to connect corresponding pairs of vertices from the pial and GM/WM boundary surface meshes. Using the MRtrix3 *tckresample* command (Tournier et al. 2019), we then partitioned each cortical column into 21 equidistant depths from the pial surface to the GM/WM boundary surface, with a step size of 5% of the cortical thickness (Waehnert et al. 2014; Waehnert et al. 2016). Note that the term *depth* as used in this context refers to the 21 equidistant partitions, rather than to a specific cortical layer (e.g. L1-L6).

Each column was also binned into one of three cortical curvature divisions: the gyral crown (threshold: -0.6 to -0.1), sulcal bank (-0.1 to 0.1), or sulcal fundus (0.1 to 0.6). These classifications were based on the FreeSurfer gaussian curvature values calculated at each vertex of the GM/WM boundary surface (Pienaar et al. 2008), with units of 1/mm². Higher values (irrespective of the sign) indicate sharper curves, and positive and negative values correspond to sulci or gyri, respectively. Based on known neuroanatomy of the human cerebral cortex (Fischl and Dale 2000), and potential atrophy related to AD, we included all columns with a biologically plausible cortical thickness value between 0.5 mm and 6 mm. Because cortical depth is measured as equidistant percentages of the cortical thickness, rather than in mm, the results of the cortical depth analyses are not affected

by differences in the degree of cortical thinning between healthy controls and participants with AD.

To obtain cortical ROIs, we parcellated each participant's brain according to the Lausanne multi-scale cortical parcellation (Cammoun et al. 2012), using the *easy_lausanne* command (https://github.com/mattcieslak/easy_lausanne), as part of the Human Connectome Mapper (Daducci et al. 2012). We used the T1-weighted anatomical image volumes and FreeSurfer tissue segmentations as inputs and the T2-weighted FLAIR image volumes (aligned to the native T1-weighted anatomical space) as the target images. This command produces five parcellations, ranging from 34 to 250 ROIs per hemisphere, but we limited all analyses to the 34 ROI parcellation that corresponds to the Desikan-Killiany atlas (Desikan et al. 2006).

Finally, for each participant, we registered their QSM image to their skull-stripped T1-weighted anatomical image volume using FSL's *flirt* with six degrees of freedom (Jenkinson et al. 2002). We then thresholded the registered susceptibility map to obtain separate signed maps of positive (e.g. iron) or negative (e.g. myelin, protein aggregation) susceptibility values, which have distinct neurobiological properties (Liu et al. 2015; Deh et al. 2018; Shin et al. 2021). For each participant, we separately sampled susceptibility values from the two signed maps for each of combination of 21 cortical depths, three curvature bins, and 34 ROIs per hemisphere.

On average, 81,233 voxels had positive susceptibility values and 76,694 voxels had negative susceptibility values, confirming that each susceptibility map contained a sufficient number of values for layer-specific sampling. We also confirmed that each ROI had sufficient voxels with positive and negative susceptibility values (Supplementary Table 1), except for positive susceptibility in the bilateral temporal pole and entorhinal cortex, negative susceptibility in the bilateral transverse temporal cortex, and both types of susceptibility for the bilateral frontal pole (~200 or fewer voxels). Results from these ROIs should be interpreted with caution.

Statistical analyses

Using a combination of R (4.3.1), MATLAB (2023a), and JASP (0.17.1), we performed statistical analyses at three different anatomical levels, the first of which was conducted at the level of *global cortical depth*. For this analysis, we averaged susceptibility values across the 34 ROIs per hemisphere and across all columns, regardless of their cortical curvature bin, separately for the 21 cortical depths and two types of susceptibility (positive, negative),

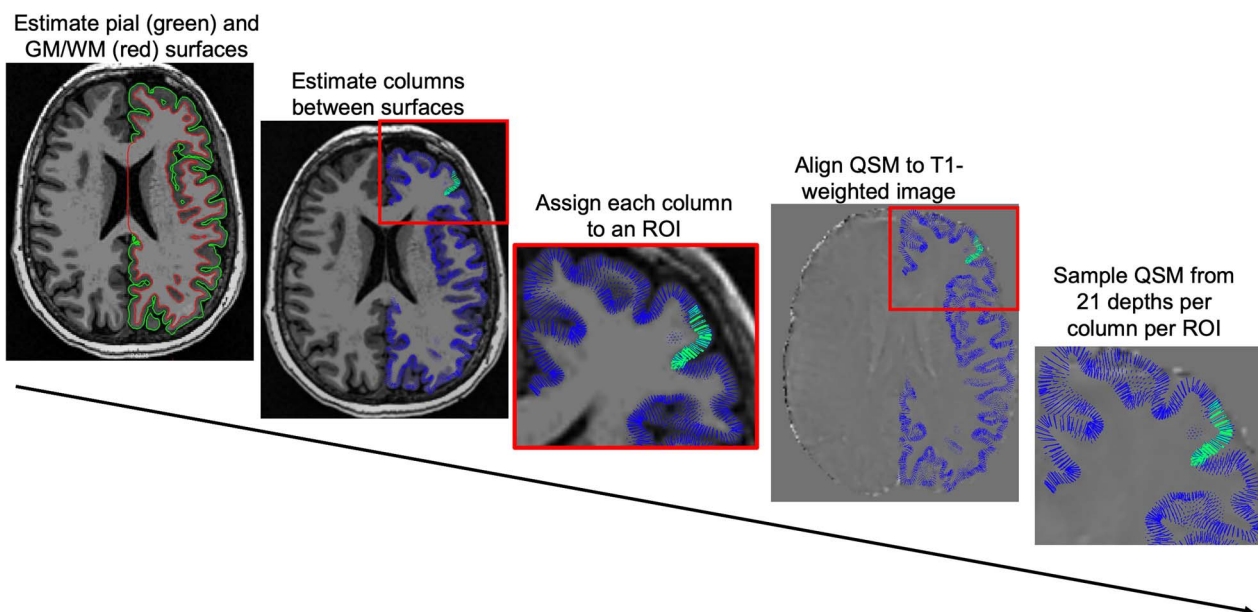


Fig. 1. Imaging data processing pipeline. All steps were performed separately for each participant in their native T1-weighted anatomical space. First, from the bias-corrected T1-weighted anatomical image volumes, FreeSurfer produces separate meshes of the pial surface and GM/WM boundary surface. Second, cortical columns are then generated by connecting corresponding pairs of vertices between the pial and GM/WM boundary surfaces. Each individual column is then assigned to one of 34 cortical ROIs per hemisphere, with an example prefrontal ROI overlaid on top of the columns. Finally, the QSM is aligned to the T1-weighted anatomical domain, and susceptibility values are sampled from 21 cortical depths per column.

resulting in a total of four unique cortical depth profiles per participant. To assess whether susceptibility varied as a function of cortical depth, and whether this relation varied as a function of group, we conducted moderation analyses in the context of ordinary linear regression (Hayes and Rockwood 2017). In these models, Depth (1–21) was the predictor variable, Group was the moderator variable, and Susceptibility (positive or negative) was the outcome variable. We used false discovery rate procedures to correct the resulting P -values for four comparisons (Benjamini and Hochberg 1995).

The second analysis was conducted at the level of *global cortical curvature*. For this analysis, we averaged susceptibility values across all 21 cortical depths and all 34 ROIs per hemisphere, but separately for each of the three curvature bins (crown, bank, fundus) and two types of susceptibility (positive, negative), resulting in a total of 12 unique values per participant. Group differences in positive or negative susceptibility between controls and participants with AD were assessed using repeated measures analyses of variance with Hemisphere and Curvature Bin as within-subjects variables and Group as a between-subjects variable. Significant main effects and interactions were probed using post hoc t -tests and the Holm-Bonferroni correction for multiple comparisons.

The final analysis was conducted at the level of *regional depth and curvature*. For this analysis, we averaged susceptibility values at each of the 21 cortical depths, within each of the 34 ROIs per hemisphere, and separately for each of the three curvature bins and two types of susceptibility. This resulted in a total of 12 unique cortical depth profiles per participant and ROI. Group differences in positive or negative susceptibility between controls and participants with AD were assessed using two-sample t -tests at each depth per ROI, using false discovery rate correction for comparisons across 21 depths.

Data availability

The data from the community-dwelling adults is not readily available on the internet because these participants did not consent to sharing their data. Demographic and MRI data for the

participants recruited from the Duke-UNC ADRC can be obtained by completing a resource request form on their website (<https://dukeuncadrc.org>). The code that was used for data analyses is available on the GitHub profile of the corresponding author.

Results

Global cortical depth-wise analyses

To assess whether susceptibility varied as a function of Cortical Depth, and whether this relation differed by Group, we created four moderation models with Depth as the predictor variable (coded as 1–21, representing the various depths from the pial surface to the GM/WM boundary), Group as the moderator variable (coded as controls = 2, AD = 1), and Susceptibility (positive or negative) from the left or right hemisphere as the outcome variable. All descriptive statistics are reported as standardized beta coefficients \pm standard error. We also conducted supplementary analyses disaggregated by cortical bin, excluding the outermost depths, to assess the potential impact of partial volume effects and minimize the number of statistical comparisons. The pattern of results did not change (Supplementary Material and Supplementary Figure 1).

Positive susceptibility

In the left hemisphere, results indicated a significant effect of Group, $\beta = -0.552 \pm 6.764 \times 10^{-5}$, $p_{FDR} < 0.001$, and Depth, $\beta = 0.919 \pm 8.518 \times 10^{-6}$, $p_{FDR} < 0.001$, as well as a significant Group \times Depth interaction, $\beta = -0.221 \pm 5.387 \times 10^{-6}$, $p_{FDR} = 0.012$ (Fig. 2A). In the right hemisphere, results similarly indicated a significant effect of Group, $\beta = -0.657 \pm 8.897 \times 10^{-5}$, $p_{FDR} < 0.001$, and Depth, $\beta = 0.660 \pm 1.120 \times 10^{-5}$, $p_{FDR} < 0.001$, as well as a significant Group \times Depth interaction, $\beta = 0.190 \pm 7.086 \times 10^{-6}$, $p_{FDR} = 0.036$ (Fig. 2B).

For both hemispheres, the main effects indicated that positive susceptibility was significantly higher for participants with AD than controls and increased from the pial surface to the GM/WM boundary. For the interaction term in the left hemisphere, follow-up Johnson-Neyman analyses (Johnson and Fay 1950) indicated

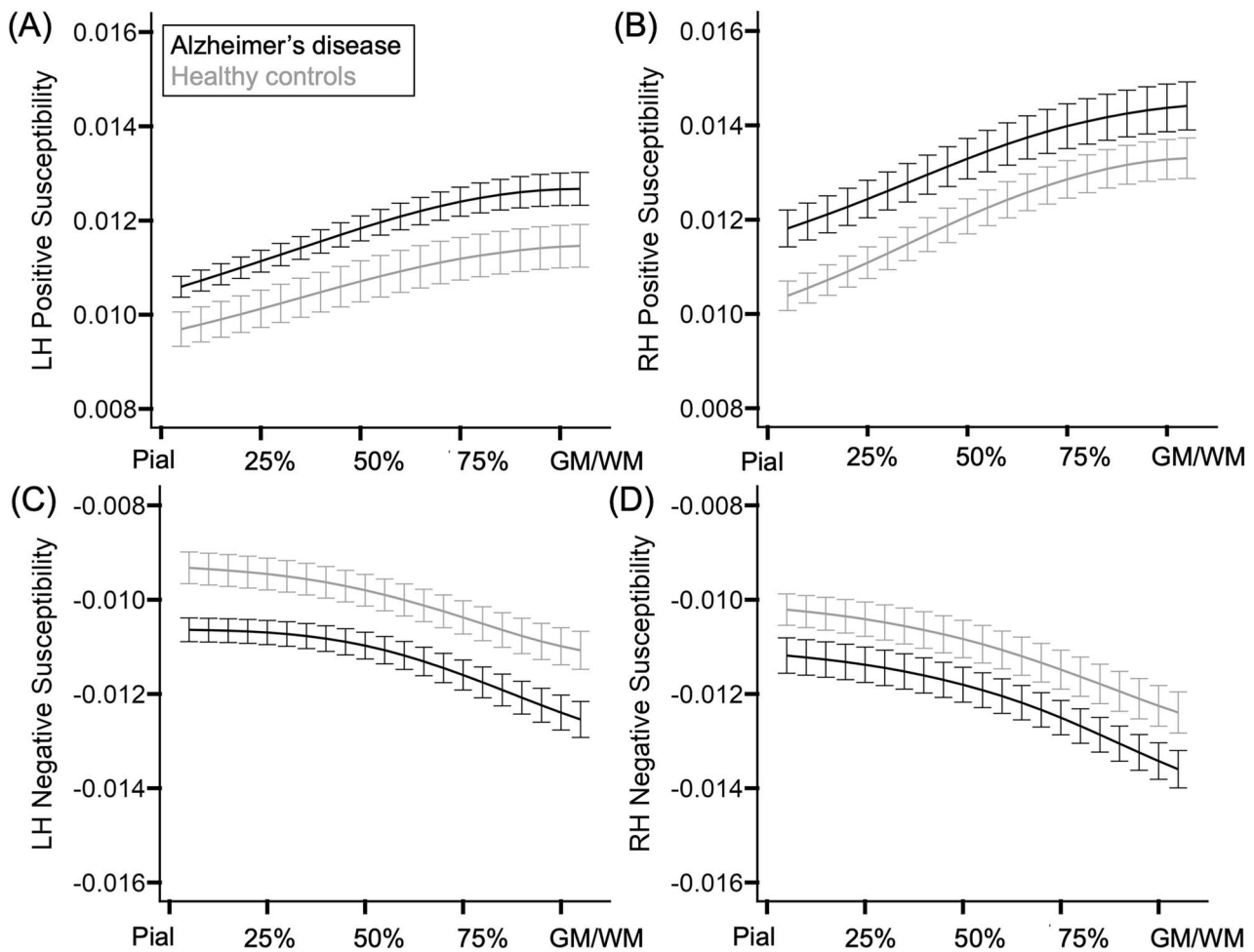


Fig. 2. Cortical depth analysis. Line graphs display positive (A, B) or negative (C, D) susceptibility as a function of cortical depth, separately for the left (LH) or right (RH) hemisphere. Participants with AD are shown in black, and control participants in gray. Error bars represent the standard error of the mean. Moderation analyses examined whether the regression coefficient (β) was significant for group, depth, and their interaction, with significant effects surviving false discovery rate correction for multiple comparisons. For both groups, there were significant increases in positive susceptibility and decreases in negative susceptibility as depth increased from the pial surface to the GM/WM boundary. For positive susceptibility, this increase was significantly larger in the LH for participants with AD and in the RH for control participants. Susceptibility is measured in parts per million (ppm).

that the relation between depth and positive susceptibility was significantly larger for participants with AD, $t(21) = 29.208$, $P < 0.001$, than controls, $t(21) = 24.782$, $P < 0.001$. In the right hemisphere, the relation between depth and positive susceptibility was instead significantly larger for controls, $t(21) = 31.224$, $P < 0.001$, than participants with AD, $t(21) = 27.472$, $P < 0.001$.

Negative susceptibility

In the left hemisphere, results indicated a significant effect of Group, $\beta = 0.691 \pm 9.765 \times 10^{-5}$, $p_{\text{FDR}} < 0.001$, and Depth, $\beta = -0.723 \pm 1.230 \times 10^{-5}$, $p_{\text{FDR}} < 0.001$ (Fig. 2C). In the right hemisphere, results similarly indicated a significant effect of Group, $\beta = 0.551 \pm 9.444 \times 10^{-5}$, $p_{\text{FDR}} < 0.001$, and Depth, $\beta = -0.907 \pm 1.189 \times 10^{-5}$, $p_{\text{FDR}} < 0.001$ (Fig. 2D). There were no significant Group \times Depth interactions for either hemisphere, $p_{\text{FDR}} \geq 0.362$.

For both hemispheres, the main effects indicated that negative susceptibility was significantly larger (i.e. more negative) for participants with AD than controls and increased from the pial surface to the GM/WM boundary.

Global cortical curvature-based analyses

To assess whether susceptibility differed as a function of Hemisphere, Cortical Curvature, and Group, we conducted two repeated

measures analyses of variance. Significant effects were probed using post hoc t-tests with the Holm-Bonferroni method applied for multiple comparisons. All descriptive statistics are reported as mean or mean difference \pm standard error.

Positive susceptibility

There were significant main effects of Group, $F(1, 42) = 5.728$, $P = 0.021$, $\eta^2_p = 0.120$, and Hemisphere, $F(1, 42) = 44.112$, $P < 0.001$, $\eta^2_p = 0.512$ (Fig. 3A and B), indicating that susceptibility was higher for participants with AD than controls ($0.001 \pm 4.805e^{-4}$) and for the right than left hemisphere ($0.001 \pm 2.099e^{-4}$). There was also a significant main effect of Curvature, $F(2, 84) = 522.260$, $P < 0.001$, $\eta^2_p = 0.926$ (Fig. 3A and B), indicating that susceptibility was higher in the crown than the bank ($0.004 \pm 1.789e^{-4}$) and fundus ($0.006 \pm 1.789e^{-4}$), and in the bank than the fundus ($0.002 \pm 1.789e^{-4}$), $t(43) \geq 9.616$, $P < 0.001$. A significant Hemisphere \times Curvature interaction, $F(2, 84) = 52.663$, $P < 0.001$, $\eta^2_p = 0.556$, indicated that susceptibility was higher in the right than left hemisphere for the crown and bank, $t(43) \geq 3.256$, $P \leq 0.003$, with no significant difference between the left and right fundus, $P = 0.051$. Finally, a significant Group \times Curvature interaction, $F(2, 84) = 5.306$, $P = 0.007$, $\eta^2_p = 0.112$, indicated that susceptibility was higher for participants with AD than controls

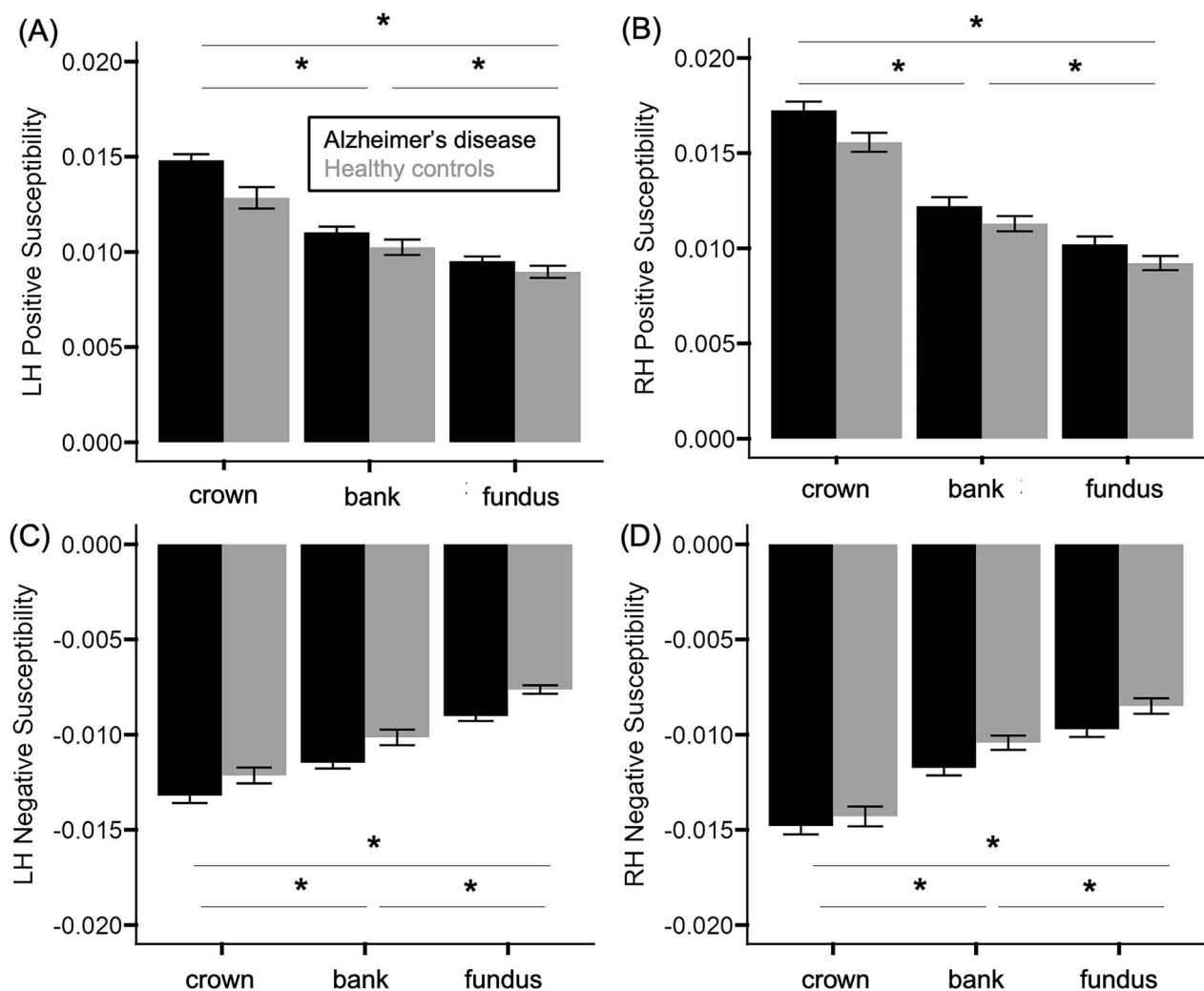


Fig. 3. Cortical curvature analysis. Bar graphs display group differences in positive (A, B) or negative (C, D) susceptibility as a function of cortical curvature (crown, bank, or fundus), separately for the left (LH) and right (RH) hemispheres. The mean values for participants with AD are displayed in black, and control participants in gray. Error bars represent the standard error of the mean. Repeated measures analyses of variance were used to examine the effect of group (between-subjects variable) and hemisphere and curvature (within-subjects variable), with significant effects surviving Holm-Bonferroni correction for multiple comparisons. For both positive and negative susceptibility, there were significantly larger values for participants with AD than controls, and for the RH than LH. For positive susceptibility, the group difference was significant for the gyral crown, but not the sulcal bank or fundus. Susceptibility is measured in parts per million (ppm).

in the gyral crown ($0.002 \pm 5.230e^{-4}$), $t(43) = 3.483$, $P = 0.004$, with no significant differences for the bank or fundus, $ps \geq 0.266$. There were no significant Group \times Hemisphere or Group \times Hemisphere \times Curvature interactions, $ps \geq 0.233$.

Negative susceptibility

There were significant main effects of Group, $F(1, 42) = 6.718$, $P = 0.013$, $\eta^2_p = 0.138$, and Hemisphere, $F(1, 42) = 21.002$, $P < 0.001$, $\eta^2_p = 0.333$ (Fig. 3C and D), indicating that susceptibility was more negative for participants with AD than controls ($-0.001 \pm 4.392e^{-4}$) and for the right than left hemisphere ($-9.760e^{-4} \pm 2.130e^{-4}$). There was also a significant main effect of Curvature, $F(2, 84) = 435.814$, $P < 0.001$, $\eta^2_p = 0.912$ (Fig. 3C and 3D), indicating that susceptibility was more negative in the crown than the bank ($-0.003 \pm 1.661e^{-4}$) and fundus ($-0.005 \pm 1.661e^{-4}$), and in the bank than the fundus ($-0.002 \pm 1.661e^{-4}$), $t(43) \geq 13.447$, $P < 0.001$. A significant Hemisphere \times Curvature interaction, $F(2, 84) = 18.484$, $P < 0.001$, $\eta^2_p = 0.306$, indicated that susceptibility was more negative in the right than left hemisphere for the crown and fundus, $t(43) \geq 2.943$, $P \leq 0.008$, with no significant

difference between the left and right bank, $P = 0.303$. There were no significant Group \times Hemisphere, Group \times Curvature, or Group \times Hemisphere \times Curvature interactions, $ps \geq 0.186$.

Regional depth- and curvature-based analyses

For each of the 34 cortical ROIs per hemisphere, we assessed group differences in positive or negative susceptibility as a function of cortical depth using two-sample t-tests. The resulting P-values were corrected for comparisons across 21 cortical depths using false discovery rate procedures within each ROI. We further disaggregated these analyses by curvature bin (crown, bank, fundus) but report these findings as exploratory due to the number of statistical comparisons required.

Positive susceptibility

Participants with AD had significantly higher values than controls for at least one combination of depth and curvature for all four lobes, primarily within the left hemisphere (Fig. 4A). This included the following regions: left prefrontal cortex (pars triangularis,

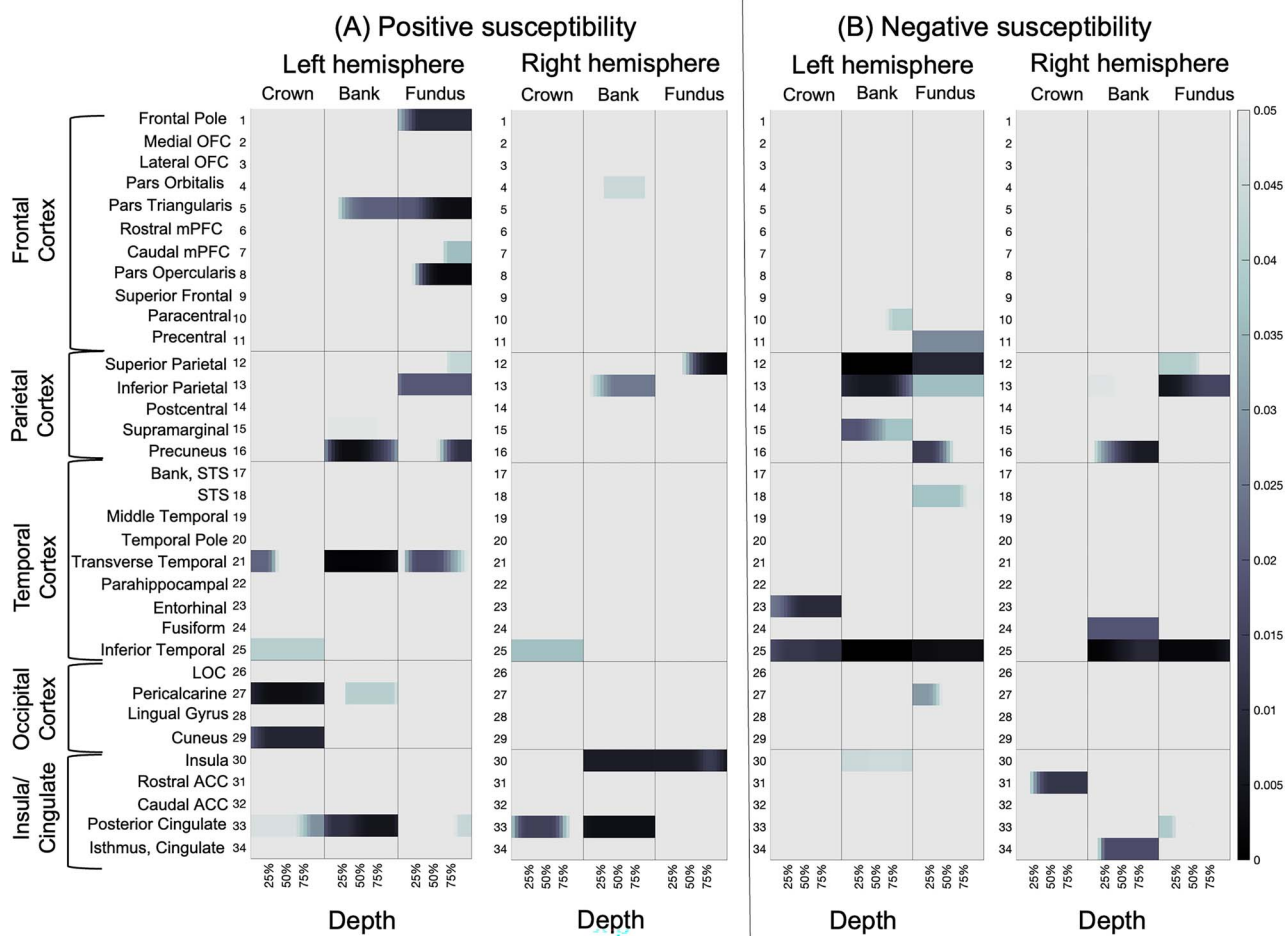


Fig. 4. Regional curvature and depth analysis. Colormaps illustrate group differences in positive (A) and negative (B) susceptibility as a function of cortical depth (from the pial surface at 0% depth through the GM/WM boundary at 100% depth), separately for each curvature bin (crown, bank, fundus) and ROI. Two-sample *t*-tests examined group differences in susceptibility at each depth, per ROI. The displayed *P*-values were corrected for comparisons across 21 cortical depths using false discovery rate procedures. All comparisons indicated significantly larger susceptibility values for adults with AD than controls, except for the left frontal pole and right pars orbitalis for positive susceptibility and the right rostral ACC for negative susceptibility. Susceptibility is measured in parts per million (ppm). OFC = orbitofrontal cortex, mPFC = middle prefrontal cortex, STS = superior temporal sulcus, LOC = lateral occipital cortex.

caudal medial prefrontal cortex, pars opercularis), bilateral superior and inferior parietal cortex, left precuneus, left transverse and bilateral inferior temporal cortex, left occipital cortex (pericalcarine cortex, cuneus), right insula, and bilateral posterior cingulate. Participants with AD had significantly lower values than controls in two frontal regions (left frontal pole and right pars orbitalis).

Analyses of depth indicated that, for both hemispheres, most regional group differences were significant across all 21 depths. Few (i.e. five) regional differences were only significant in deeper depths (i.e. 50% depth to the GM/WM boundary).

Exploratory analyses of curvature indicated that most regional group differences were significant in sulci (bank, fundus). Specifically, significant differences were only observed in the sulci for the prefrontal (left frontal pole, pars triangularis, pars opercularis, caudal medial prefrontal cortex, and right pars orbitalis), right insula, and parietal (left precuneus, bilateral superior and inferior parietal cortex) ROIs. Differences were only observed in the gyri for the bilateral inferior temporal and left cuneus ROIs. Differences were observed in both the gyri and sulci for the left transverse temporal, left pericalcarine, and bilateral posterior cingulate ROIs.

Negative susceptibility

Participants with AD had significantly more negative values than controls for at least one combination of depth and curvature, primarily within the bilateral temporal and parietal lobes (Fig. 4B). This included the following regions: left paracentral and precentral cortex, bilateral superior and inferior parietal cortex, left supramarginal, bilateral precuneus, left superior temporal, left entorhinal cortex, right fusiform, bilateral inferior temporal cortex, left pericalcarine cortex, left insula, and the right posterior cingulate and isthmus of the cingulate. Participants with AD had significantly lower values than controls in the right rostral anterior cingulate (ACC).

Analyses of depth indicated that, for both hemispheres, most regional group differences were significant across all 21 depths. Few (i.e. five) regional differences were only significant in superficial depths (i.e. pial surface through 50% depth).

Exploratory analyses of curvature indicated that most regional group differences were significant in sulci (bank, fundus). Specifically, significant differences were only observed in the sulci for the left paracentral and precentral cortex, bilateral superior and inferior parietal cortex, left supramarginal, bilateral precuneus,

left superior temporal, right fusiform, right inferior temporal cortex, left pericalcarine cortex, left insula, and the right posterior cingulate and isthmus of the cingulate. Differences were only observed in the gyri for left entorhinal cortex and right rostral ACC. Differences were observed in both the gyri and sulci for the left inferior temporal cortex.

Discussion

Previous QSM studies have identified excessive cortical iron accumulation in AD, but these studies used more macroscopic analytical approaches that offer limited anatomical specificity. To extend prior research, the current QSM study conducted depth-wise and curvature-based analyses of cortical iron accumulation (positive susceptibility), among other neural substrates (negative susceptibility), in AD. As expected, cortical iron content was significantly higher for adults with AD relative to healthy controls. Overall iron content increased from superficial to deeper depths (i.e. from the pial surface to the GM/WM boundary) and was higher in gyri than sulci. Relative to controls, adults with AD exhibited a larger linear effect of depth on cortical iron accumulation in the left hemisphere and higher iron in the gyral crown. At the regional level, most of the significant group differences in iron content were found across all cortical depths, although exploratory analyses suggested that some of these effects may be limited to specific curvature bins. These findings suggest that iron accumulates in a topographically heterogeneous manner across the cortical mantle in AD.

Global depth-wise analyses

Across groups, cortical iron content increased from superficial (i.e. toward the pial surface) to deeper (i.e. toward the GM/WM boundary) depths (Fig. 2A and B). This finding is in line with one prior depth-wise study of middle frontal and precentral regions in healthy younger adults (Lee et al. 2023) and ex vivo studies of human brain tissue reporting lower susceptibility in superficial layers and higher susceptibility in deeper layers (Fukunaga et al. 2010; Shin et al. 2020). Extending prior work, we found that adults with AD had higher cortical iron content than controls, with a larger linear depth-wise increase in the left hemisphere. In contrast, the slope of the depth-wise increase in cortical iron for the right hemisphere was significantly larger for controls, but overall iron content was still lower than for adults with AD. One prior voxelwise study similarly reported a left hemisphere dominance of cortical iron accumulation in AD (Yang et al. 2022), mirroring the larger disease-related effects for GM atrophy (Plocharski and Østergaard 2016), cortical thinning (Roe et al. 2021), and metabolic dysfunction (Loewenstein et al. 1989) in the left hemisphere. The left hemisphere may therefore be more vulnerable to iron accumulation across cortical depths in AD, but more resistant to this accumulation in healthy aging.

In exploratory analyses, we found that negative susceptibility similarly increased from superficial to deeper cortical depths (Fig. 2C and D), replicating prior depth-wise studies of healthy younger (Lee et al. 2023) and older (Northall et al. 2023) adults. Finding that negative susceptibility peaks at the GM/WM boundary is expected if this measure is sensitive to myelin (Hametner et al. 2018; Kirilina et al. 2020), which is much higher in the dense fiber bundles of WM compared to the less myelinated axons of GM (Oost et al. 2023). We also observed, however, that even in the face of demyelination (Bouhrara et al. 2018; Veale et al. 2021), adults with AD exhibited more negative susceptibility across cortical depths (i.e. more diamagnetic substance) when

compared to controls. It is important to note that the precise sources of negative susceptibility are still under debate (Duyn and Schenck 2017; Gong et al. 2019; Lazari and Lipp 2021; Zhao et al. 2021) and may also reflect the accumulation of calcium (Kim et al. 2020) and $A\beta$ (Gong et al. 2019; Zhao et al. 2021). Thus, the group difference in negative susceptibility is likely driven by a combination of multiple diamagnetic neural properties that cannot be disentangled in the current study.

Global curvature-based analyses

The curvature-based analyses indicated that cortical iron content was higher in gyri relative to sulci, in adults with AD relative to controls, and in the right hemisphere relative to left (Fig. 3A and B). The overall difference in iron content for gyri versus sulci may reflect their greater cortical thickness (Fischl and Dale 2000), resulting in a larger area for iron to distribute (Hernández-Torres et al. 2019; Taege et al. 2019). In contrast to the depth-wise analyses, the absence of a Group \times Hemisphere interaction indicated that the pattern of AD-related iron accumulation in the three curvature bins was comparable between the left and right hemispheres. A significant Group \times Curvature interaction indicated that global iron content was significantly higher in gyri, but comparable in sulci, for adults with AD relative to controls. We expected to observe group differences in iron in sulci rather than in gyri because the sulci exhibit more pronounced atrophy in AD (Im et al. 2008; Liu et al. 2013; Hamelin et al. 2015; Plocharski and Østergaard 2016) and are more vulnerable to $A\beta$ and tau accumulation (Clinton et al. 1993; Arendt et al. 2017). However, any interactive effect between neurodegeneration and iron accumulation in sulci may also be present in controls, as some degree of sulcal atrophy is also a feature of healthy aging (Lin et al. 2021). Gyri may also be uniquely vulnerable to iron accumulation in AD due to layer-specific differences in thickness (i.e. thicker superficial layers in sulci relative to thicker deep layers in gyri) and the type and density of neurons (Bok 1929; Waehnert et al. 2014; Consolini et al. 2022).

The exploratory curvature-based analyses of negative susceptibility also indicated larger values in gyri relative to sulci, in adults with AD relative to controls, and in the right hemisphere relative to left (Fig. 3C and D). There is some evidence that $A\beta$ exhibits diamagnetic properties, which would increase negative susceptibility in adults with AD (Gong et al. 2019; Zhao et al. 2021), especially in sulci (Clinton et al. 1993; Arendt et al. 2017). However, the lack of any interaction with group suggests that the difference in negative susceptibility was comparable across curvature bins and hemispheres. The role of neuropathologies in curvature-specific group differences in negative susceptibility can be tested directly in future studies conducting column-based QSM analyses in combination with positron emission tomography measures of $A\beta$ or tau (Cogswell and Fan 2023).

Regional analyses

Conducting depth-wise and curvature-based analyses at the regional level may provide complementary results to the global analyses as subregions of the cortex exhibit heterogeneous cytoarchitecture (Brodmann 1909) and may not be equally affected by AD (Dickerson et al. 2009). Indeed, we found that adults with AD exhibited higher iron content than controls in subregions of the four lobes (Fig. 4A), including the right insula, bilateral posterior parietal cortex, and bilateral posterior cingulate (Dai et al. 2014; Bertolero et al. 2018; Clarke et al. 2022; Dadario and Sughrue 2023). These highly interconnected hub regions are among the first to accumulate $A\beta$ and have

been implicated in the manifestation of AD by morphometric, functional, and metabolic studies (Walhovd et al. 2010; Anthony and Lin 2017; Henf et al. 2018). Interestingly, most of the regional differences in iron content were present within sulci which differs from the group difference in global iron content observed within the gyral crown. While speculative, one interpretation of this finding is that the sulci-specific regional effects may be driven by the local accumulation of AD-related pathology. Nonetheless, taken together with earlier work (Zhu et al. 2009; Acosta-Cabronero et al. 2013; Kim et al. 2017; Yang et al. 2022), the current finding suggests that iron burden in these regions may also play an important role in disease manifestation.

Most regional differences in iron load were present across all 21 depths, apart from a few regions that only differed at deeper depths (50% depth to the GM/WM boundary). One depth-wise study of healthy younger and older adults similarly observed age group differences in susceptibility across all depths of the primary motor cortex, although there was a larger age group difference within superficial depths (Northall et al. 2023). But a separate depth-wise study of healthy older adults examining myelin content across the entire cortex observed that most age-related variance in depth-wise myelin profiles was driven by deeper, rather than superficial, depths (Sui et al. 2022). Taken together, these findings suggest that depth-specific differences in iron content, among other neural properties, may be a feature unique to healthy aging but not AD. Future work should aim to bridge these two literatures to characterize depth-specific differences in iron content across the entire cortex in healthy aging, especially in combination with measures of cognitive performance. Because cognitive decline in healthy older adults is dominated by slowing of response-related processes relative to decision-related processes (Ratcliff 2008; Madden et al. 2020; Merenstein et al. 2023), one might predict that most regional age-related differences in iron content are present in deep layers responsible for output functions, instead of superficial layers responsible for integrating information from other regions (Rolls and Mills 2017). Nonetheless, our current finding of higher iron across all depths may help explain the additional cognitive deficits in AD, beyond the more general age-related slowing of motor responses that is also observed in healthy aging.

The regional analyses further suggest that the separation of positive and negative susceptibility is valuable for assessing distinct neural properties (Fig. 4B), as some regions only showed a significant difference for one type of susceptibility (e.g. right fusiform, left entorhinal cortex). Other regions showed significant group differences for both types of susceptibility (e.g. bilateral superior and inferior parietal cortex, bilateral inferior temporal cortex), suggesting that some regions may be vulnerable to the accumulation of both iron and neuropathologies (van Bergen et al. 2016; Spotorno et al. 2020). Most regional group differences in negative susceptibility were again only present in sulci but across all 21 depths, apart from a few regions that only differed at superficial depths (pial surface to 50% depth). Assuming that negative susceptibility is at least partly sensitive to $A\beta$, both of these findings are expected because $A\beta$ is more prominent in sulci relative to gyri (Clinton et al. 1993; Arendt et al. 2017), in superficial relative to deeper layers (Kraszpulski et al. 2001; Romito-DiGiacomo et al. 2007; Edler et al. 2023), and in temporal-parietal regions (Braak and Braak 1991).

Strengths and limitations

These column-based analyses provide detailed anatomical information that cannot be achieved using voxelwise or whole ROI

approaches. The sensitivity of QSM data to depth-specific group differences in susceptibility may be increased in future work by increasing the spatial resolution (e.g. 0.5 mm; Northall et al. 2023). Higher resolution data can help reduce partial volume effects and clarify the specificity of iron accumulation in specific depths and curvature bins, although these sequences typically require partial rather than whole-brain coverage, as was acquired here. A limitation of the column-based approach is that it is not appropriate for deep GM nuclei because these nuclei are a dense collection of cell bodies that do not exhibit a specific laminar structure. The current study therefore cannot compare the anatomical distribution of iron in deep GM nuclei to cortical regions, even though these nuclei accumulate much higher amounts of iron (Hallgren and Sourander 1958). We also did not acquire positron emission tomography scans from the current sample, although the majority of patient diagnoses were defined by fluid-based biomarkers. In combination with a cross-sectional design, we therefore cannot identify how iron may be colocalizing with neuropathologies ($A\beta$, tau) across cortical layers. Nonetheless, future investigations can conduct these column-based analyses on other clinically feasible MRI sequences, such as diffusion tensor imaging of cortical microstructure (Ma et al. 2023). Finally, in contrast to the binarization approach used here, future work could use the DECOMPOSE-QSM algorithm, which uses the phase and magnitude information from a GRE acquisition sequence to separately estimate paramagnetic and diamagnetic susceptibility within each voxel (Chen et al. 2021) and has been successfully applied to study neurodegeneration in AD (Ahmed et al. 2023).

Conclusions

The current study sought to characterize iron accumulation as a function of cortical depth and curvature in adults with AD. Relative to healthy age- and sex-matched controls, adults with AD exhibited unique anatomical variation in global positive susceptibility (a proxy for brain iron content) in gyri and across superficial and deeper cortical depths. Regional group differences in iron content were most prominent in higher-order cortical regions and in sulci. These accentuated depth-wise and curvature-specific group differences in iron load may help explain the profound cognitive deterioration that differentiates AD from the general slowing of elementary motor processes in healthy aging. Findings from this study should be informative for future multimodal analyses combining column-based information of QSM with other neuroimaging measures or behavioral measures of cognitive performance.

Acknowledgments

We are grateful to Yixin Ma, Cortney Howard, Hollie Mullin, and Matthew Wang for their assistance with this project. The address of the corresponding author is: Brain Imaging and Analysis Center, Box 3918, Duke University Medical Center, Durham, NC, 27710, email: jenna.merenstein@duke.edu.

Author contributions

Jenna Merenstein (Conceptualization, Data curation, Formal analysis, Investigation, Methodology, Project administration, Validation, Visualization, Writing—original draft, Writing—review & editing), Jiayi Zhao (Formal analysis, Methodology, Software, Writing—review & editing), Devon Overson (Methodology, Resources, Software, Validation, Writing—review & editing), Trong-Kha Truong (Funding acquisition, Methodology, Resources, Software,

Supervision, Validation, Writing—review & editing), Kim Johnson (Methodology, Project administration, Resources, Writing—review & editing), Allen Song (Conceptualization, Funding acquisition, Methodology, Supervision, Writing—review & editing), and David Madden (Conceptualization, Funding acquisition, Investigation, Methodology, Project administration, Resources, Software, Supervision, Writing—original draft, Writing—review & editing).

Supplementary material

Supplementary material is available at *Cerebral Cortex* online.

Funding

This work was supported by the National Institutes of Health under Award Numbers R01 AG039684, R56 AG052576, R01 EB028644, and P30 AG072958.

Conflict of interest statement: None declared.

References

- Acosta-Cabronero J, Williams GB, Cardenas-Blanco A, Arnold RJ, Lupson V, Nestor PJ. In vivo quantitative susceptibility mapping (QSM) in Alzheimer's disease. *PLoS One*. 2013;8(11):e81093.
- Acosta-Cabronero J, Betts MJ, Cardenas-Blanco A, Yang S, Nestor PJ. In vivo MRI mapping of brain iron deposition across the adult lifespan. *J Neurosci*. 2016;36(2):364–374.
- Ahmed M, Chen J, Arani A, Senjem ML, Cogswell PM, Jack CR Jr, Liu C. The diamagnetic component map from quantitative susceptibility mapping (QSM) source separation reveals pathological alteration in Alzheimer's disease-driven neurodegeneration. *NeuroImage*. 2023;280:120357.
- Anthony M, Lin F. A systematic review for functional neuroimaging studies of cognitive reserve across the cognitive aging spectrum. *Arch Clin Neuropsychol*. 2017;33(8):937–948.
- Arendt T, Morawski M, Gärtner U, Fröhlich N, Schulze F, Wohmann N, Jäger C, Eisenlöffel C, Gertz H-J, Mueller W, et al. Inhomogeneous distribution of Alzheimer pathology along the isocortical relief. Are cortical convolutions an Achilles heel of evolution? *Brain Pathol*. 2017;27(5):603–611.
- Avants BB, Tustison NJ, Song G, Cook PA, Klein A, Gee JC. A reproducible evaluation of ANTs similarity metric performance in brain image registration. *NeuroImage*. 2011;54(3):2033–2044.
- Bach M. The Freiburg visual acuity test - automatic measurement of visual acuity. *Optom Vis Sci*. 1996;73(1):49–53.
- Beck AT. *The Beck depression inventory*. New York: Psychological Corporation; 1978.
- Benjamini Y, Hochberg Y. Controlling the false discovery rate: a practical and powerful approach to multiple testing. *J Roy Stat Soc Ser B (Stat Method)*. 1995;57(1):289–300.
- Bertolero MA, Yeo BTT, Bassett DS, D'Esposito M. A mechanistic model of connector hubs, modularity and cognition. *Nat Hum Behav*. 2018;2(10):765–777.
- Besser L, Kukull W, Knopman DS, Chui H, Galasko D, Weintraub S, Jicha G, Carlsson C, Burns J, Quinn J, et al. Version 3 of the National Alzheimer's coordinating Center's uniform data set. *Alzheimer Dis Assoc Disord*. 2018;32(4):351–358.
- Bok ST. [The influence of the curvatures of the cerebral cortex occurring in the furrows and convolutions on the cortical architecture]. *Der Einfluder in den Furchen und Windungen auftretenden Krümmungen der Grohirnrinde auf die Rindenarchitektur*. *Zeitschrift für die gesamte Neurologie und Psychiatrie*. 1929;121(1):682–750.
- Bouhrara M, Reiter DA, Bergeron CM, Zukley LM, Ferrucci L, Resnick SM, Spencer RG. Evidence of demyelination in mild cognitive impairment and dementia using a direct and specific MRI measure of myelin content. *Alzheimers Dement*. 2018;14(8):998–998, 1004.
- Braak H, Braak E. Neuropathological staging of Alzheimer-related changes. *Acta Neuropathol*. 1991;82(4):239–259.
- Brodmann K. Localization in the cerebral cortex. In: *Vergleichende Lokalisationslehre der Grosshirnrinde in ihren Prinzipien dargestellt auf Grund des Zellenbaues*. Leipzig: Barth; 1909.
- Bulk M, Kenkhuis B, van der Graaf LM, Goeman JJ, Natté R, van der Weerd L. Postmortem T2*-weighted MRI imaging of cortical iron reflects severity of Alzheimer's disease. *J Alzheimers Dis*. 2018;65(4):1125–1137.
- Cammoun L, Gigandet X, Meskaldji D, Thiran JP, Sporns O, Do KQ, Maeder P, Meuli R, Hagmann P. Mapping the human connectome at multiple scales with diffusion spectrum MRI. *J Neurosci Methods*. 2012;203(2):386–397.
- Chen J, Gong N-J, Chaim KT, Otaduy MCG, Liu C. Decompose quantitative susceptibility mapping (QSM) to sub-voxel diamagnetic and paramagnetic components based on gradient-echo MRI data. *NeuroImage*. 2021;242:118477.
- Clarke H, Messaritaki E, Dimitriadis SI, Metzler-Baddeley C. Dementia risk factors modify hubs but leave other connectivity measures unchanged in asymptomatic individuals: a graph theoretical analysis. *Brain Connect*. 2022;12(1):26–40.
- Clinton J, Roberts GW, Gentleman SM, Royston MC. Differential pattern of β -amyloid protein deposition within cortical sulci and gyri in Alzheimer's disease. *Neuropathol Appl Neurobiol*. 1993;19(3):277–281.
- Cogswell PM, Fan AP. Multimodal comparisons of QSM and PET in neurodegeneration and aging. *NeuroImage*. 2023;120068:120068.
- Consolini J, Demirci N, Fulwider A, Hutsler JJ, Holland MA. Bok's equivolume principle: translation, historical context, and a modern perspective. *Brain Multiphys*. 2022;3:100057.
- Cummings JL, Mega M, Gray K, Rosenberg-Thompson S, Carusi DA, Gornbein J. The neuropsychiatric inventory: comprehensive assessment of psychopathology in dementia. *Neurology*. 1994;44(12):2308–2314.
- Dadario NB, Sughrue ME. The functional role of the precuneus. *Brain*. 2023;146(9):3598–3607.
- Daducci A, Gerhard S, Griffa A, Lemkaddem A, Cammoun L, Gigandet X, Meuli R, Hagmann P, Thiran J-P. The connectome mapper: an open-source processing pipeline to map connectomes with MRI. *PLoS One*. 2012;7(12):e48121.
- Dai Z, Yan C, Li K, Wang Z, Wang J, Cao M, Lin Q, Shu N, Xia M, Bi Y, et al. Identifying and mapping connectivity patterns of brain network hubs in Alzheimer's disease. *Cereb Cortex*. 2014;25(10):3723–3742.
- Daugherty AM, Raz N. Appraising the role of iron in brain aging and cognition: promises and limitations of MRI methods. *Neuropsychol Rev*. 2015;25(3):272–287.
- Deh K, Ponath GD, Molvi Z, Parel GT, Gillen KM, Zhang S, Nguyen TD, Spincemaille P, Ma Y, Gupta A, et al. Magnetic susceptibility increases as diamagnetic molecules breakdown: myelin digestion during multiple sclerosis lesion formation contributes to increase on QSM. *J Magn Reson Imaging*. 2018;48(5):1281–1287.
- Desikan RS, Ségonne F, Fischl B, Quinn BT, Dickerson BC, Blacker D, Buckner RL, Dale AM, Maguire RP, Hyman BT, et al. An automated labeling system for subdividing the human cerebral cortex

- on MRI scans into gyral based regions of interest. *NeuroImage*. 2006;31(3):968–980.
- Dickerson BC, Bakkour A, Salat DH, Feczko E, Pacheco J, Greve DN, Grodstein F, Wright CI, Blacker D, Rosas HD, et al. The cortical signature of Alzheimer's disease: regionally specific cortical thinning relates to symptom severity in very mild to mild AD dementia and is detectable in asymptomatic amyloid-positive individuals. *Cereb Cortex*. 2009;19(3):497–510.
- Duce JA, Tsatsanis A, Cater MA, James SA, Robb E, Wikke K, Leong SL, Perez K, Johanssen T, Greenough MA, et al. Iron-export ferroxidase activity of β -amyloid precursor protein is inhibited by zinc in Alzheimer's disease. *Cell*. 2010;142(6):857–867.
- Duyn JH, Schenck J. Contributions to magnetic susceptibility of brain tissue. *NMR Biomed*. 2017;30(4):e3546.
- Edler MK, Munger EL, Maycon H, Hopkins WD, Hof PR, Sherwood CC, Raghanti MA. The association of astrogliosis and microglial activation with aging and Alzheimer's disease pathology in the chimpanzee brain. *J Neurosci Res*. 2023;101(6):881–900.
- Fischl B, Dale AM. Measuring the thickness of the human cerebral cortex from magnetic resonance images. *Proc Natl Acad Sci U S A*. 2000;97(20):11050–11055.
- Fischl B, Sereno MI, Tootell RB, Dale AM. High-resolution intersubject averaging and a coordinate system for the cortical surface. *Hum Brain Mapp*. 1999;8(4):272–284.
- Förstl H, Kurz A. Clinical features of Alzheimer's disease. *Eur Arch Psychiatry Clin Neurosci*. 1999;249(6):288–290.
- Fukunaga M, Li TQ, van Gelderen P, de Zwart JA, Shmueli K, Yao B, Lee J, Maric D, Aronova MA, Zhang G, et al. Layer-specific variation of iron content in cerebral cortex as a source of MRI contrast. *Proc Natl Acad Sci U S A*. 2010;107(8):3834–3839.
- Gong N-J, Dibb R, Bulk M, van der Weerd L, Liu C. Imaging beta amyloid aggregation and iron accumulation in Alzheimer's disease using quantitative susceptibility mapping MRI. *NeuroImage*. 2019;191:176–185.
- Grundke-Iqbal I, Fleming J, Tung YC, Lassmann H, Iqbal K, Joshi JG. Ferritin is a component of the neuritic (senile) plaque in Alzheimer dementia. *Acta Neuropathol*. 1990;81(2):105–110.
- Haacke EM, Cheng NYC, House MJ, Liu Q, Neelavalli J, Ogg RJ, Khan A, Ayaz M, Kirsch W, Obenaus A. Imaging iron stores in the brain using magnetic resonance imaging. *Magn Reson Imaging*. 2005;23(1):1–25.
- Hallgren B, Sourander P. The effect of age on the non-haemin iron in the human brain. *J Neurochem*. 1958;3(1):41–51.
- Hamelin L, Bertoux M, Bottlaender M, Corne H, Lagarde J, Hahn V, Mangin JF, Dubois B, Chupin M, de Souza LC, et al. Sulcal morphology as a new imaging marker for the diagnosis of early onset Alzheimer's disease. *Neurobiol Aging*. 2015;36(11):2932–2939.
- Hametner S, Endmayr V, Deistung A, Palmrich P, Prihoda M, Haimburger E, Menard C, Feng X, Haider T, Leisser M, et al. The influence of brain iron and myelin on magnetic susceptibility and effective transverse relaxation - a biochemical and histological validation study. *NeuroImage*. 2018;179:117–133.
- Hayes AF, Rockwood NJ. Regression-based statistical mediation and moderation analysis in clinical research: observations, recommendations, and implementation. *Behav Res Ther*. 2017;98:39–57.
- Henf J, Grothe MJ, Brueggen K, Teipel S, Dyrba M. Mean diffusivity in cortical gray matter in Alzheimer's disease: the importance of partial volume correction. *NeuroImage Clin*. 2018;17:579–586.
- Hernández-Torres E, Wiggermann V, Machan L, Sadovnick AD, Li DKB, Traboulsee A, Hametner S, Rauscher A. Increased mean R2* in the deep gray matter of multiple sclerosis patients: have we been measuring atrophy? *J Magn Reson Imaging*. 2019;50(1):201–208.
- Howard CM, Jain S, Cook AD, Packard LE, Mullin HA, Nk C, Liu C, Song AW, Madden DJ. Cortical iron mediates age-related decline in fluid cognition. *Hum Brain Mapp*. 2022;43(3):1047–1060.
- Im K, Lee JM, Seo SW, Hyung Kim S, Kim SI, Na DL. Sulcal morphology changes and their relationship with cortical thickness and gyral white matter volume in mild cognitive impairment and Alzheimer's disease. *NeuroImage*. 2008;43(1):103–113.
- Jack CR, Bennett DA, Blennow K, Carrillo MC, Dunn B, Haeberlein SB, Holtzman DM, Jagust W, Jessen F, Karlawish J, et al. NIA-AA research framework: toward a biological definition of Alzheimer's disease. *Alzheimers Dement*. 2018;14(4):535–562.
- Jenkinson M, Bannister P, Brady M, Smith S. Improved optimization for the robust and accurate linear registration and motion correction of brain images. *NeuroImage*. 2002;17(2):825–841.
- Johnson PO, Fay LC. The Johnson-Neyman technique, its theory and application. *Psychometrika*. 1950;15(4):349–367.
- Kim HG, Park S, Rhee HY, Lee KM, Ryu CW, Rhee SJ, Lee SY, Wang Y, Jahng GH. Quantitative susceptibility mapping to evaluate the early stage of Alzheimer's disease. *NeuroImage Clin*. 2017;16:429–438.
- Kim S, Lee Y, Jeon CY, Kim K, Jeon Y, Jin YB, Oh S, Lee C. Quantitative magnetic susceptibility assessed by 7T magnetic resonance imaging in Alzheimer's disease caused by streptozotocin administration. *Quant Imaging Med Surg*. 2020;10(3):789–797.
- Kirilina E, Helbling S, Morawski M, Pine K, Reimann K, Jankuhn S, Dinse J, Deistung A, Reichenbach JR, Trampel R, et al. Superficial white matter imaging: contrast mechanisms and whole-brain in vivo mapping. *Sci Adv*. 2020;6(41):eaa9281.
- Kraszpulski M, Soininen H, Helisalms I, Alafuzoff I. The load and distribution of β -amyloid in brain tissue of patients with Alzheimer's disease. *Acta Neurol Scand*. 2001;103(2):88–92.
- Kuchcinski G, Patin L, Lopes R, Leroy M, Delbeuck X, Rollin-Sillaire A, Lebouvier T, Wang Y, Spincemaille P, Tourdias T, et al. Quantitative susceptibility mapping demonstrates different patterns of iron overload in subtypes of early-onset Alzheimer's disease. *Eur Radiol*. 2023;33(1):184–195.
- Lazari A, Lipp I. Can MRI measure myelin? Systematic review, qualitative assessment, and meta-analysis of studies validating microstructural imaging with myelin histology. *NeuroImage*. 2021;230:117744.
- Lee S, Shin HG, Kim M, Lee J. Depth-wise profiles of iron and myelin in the cortex and white matter using chi-separation: a preliminary study. *NeuroImage*. 2023;273:120058.
- Lei D, Zifang Z, Zifang Z, Zifang Z, Ailing C, Ai-Ling C, Yijiang Z, Lu Z, Jing L, Sumin S, et al. Increased iron deposition on brain quantitative susceptibility mapping correlates with decreased cognitive function in Alzheimer's disease. *ACS Chem Neurosci*. 2018;9(7):1849–1857.
- Li W, Wu B, Liu C. Quantitative susceptibility mapping of human brain reflects spatial variation in tissue composition. *NeuroImage*. 2011;55(4):1645–1656.
- Li W, Avram AV, Wu B, Xiao X, Liu C. Integrated Laplacian-based phase unwrapping and background phase removal for quantitative susceptibility mapping. *NMR Biomed*. 2014;27(2):219–227.
- Lin H-Y, Huang C-C, Chou K-H, Yang AC, Lo C-YZ, Tsai S-J, Lin C-P. Differential patterns of gyral and sulcal morphological changes during normal aging process. *Front Aging Neurosci*. 2021;13:625931.
- Liu T, Lipnicki DM, Zhu W, Tao D, Zhang C, Cui Y, Jin JS, Sachdev PS, Wen W. Cortical gyrification and sulcal spans in early stage Alzheimer's disease. *PLoS One*. 2012;7(2):e31083.

- Liu T, Sachdev PS, Lipnicki DM, Jiang J, Cui Y, Kochan NA, Reppermund S, Trollor JN, Brodaty H, Wen W. Longitudinal changes in sulcal morphology associated with late-life aging and MCI. *NeuroImage*. 2013;74:337–342.
- Liu C, Li W, Tong KA, Yeom KW, Kuzminski S. Susceptibility-weighted imaging and quantitative susceptibility mapping in the brain. *J Magn Reson Imaging*. 2015;42(1):23–41.
- Loewenstein DA, Barker WW, Chang J-Y, Apicella A, Yoshii F, Kothari P, Levin B, Duara R. Predominant left hemisphere metabolic dysfunction in dementia. *Arch Neurol*. 1989;46(2):146–152.
- Long H, Zhu W, Wei L, Zhao J. Iron homeostasis imbalance and ferroptosis in brain diseases. *MedComm*. 2023;4(4):e298.
- Lovell MA, Robertson JD, Teesdale WJ, Campbell JL, Markesbery WR. Copper, iron and zinc in Alzheimer's disease senile plaques. *J Neurol Sci*. 1998;158(1):47–52.
- Ma Y, Bruce IP, Yeh C-H, Petrella JR, Song AW, Truong T-K. Column-based cortical depth analysis of the diffusion anisotropy and radiality in submillimeter whole-brain diffusion tensor imaging of the human cortical gray matter in vivo. *NeuroImage*. 2023;270:119993.
- Madden DJ, Merenstein JL. Quantitative susceptibility mapping of brain iron in healthy aging and cognition. *NeuroImage*. 2023;282:120401.
- Madden DJ, Siciliano RE, Tallman CW, Monge ZA, Voss A, Cohen JR. Response-level processing during visual feature search: effects of frontoparietal activation and adult age. *Atten Percept Psychophys*. 2020;82(1):330–330, 349.
- Merenstein JL, Mullin HA, Madden DJ. Age-related differences in frontoparietal activation for target and distractor singletons during visual search. *Atten Percept Psychophys*. 2023;85(3):749–768.
- Morris JC. The clinical dementia rating (CDR): current version and scoring rules. *Neurology*. 1993;43(11):2412–2414.
- Nasreddine ZS, Phillips NA, Bédirian V, Charbonneau S, Whitehead V, Collin I, Cummings JL, Chertkow H. The Montreal cognitive assessment, MoCA: a brief screening tool for mild cognitive impairment. *J Am Geriatr Soc*. 2005;53(4):695–699.
- Northall A, Doehler J, Weber M, Vielhaber S, Schreiber S, Kuehn E. Layer-specific vulnerability is a mechanism of topographic map aging. *Neurobiol Aging*. 2023;128:17–32.
- Oost W, Huitema AJ, Kats K, Giepmans BNG, Kooistra SM, Eggen BJL, Baron W. Pathological ultrastructural alterations of myelinated axons in normal appearing white matter in progressive multiple sclerosis. *Acta Neuropathol Commun*. 2023;11(1):100.
- Pfeffer RI, Kurosaki TT, Harrah CH Jr, Chance JM, Filos S. Measurement of functional activities in older adults in the community. *J Gerontol*. 1982;37(3):323–329.
- Pienaar R, Fischl B, Caviness V, Makris N, Grant PE. A methodology for analyzing curvature in the developing brain from preterm to adult. *Int J Imaging Syst Technol*. 2008;18(1):42–68.
- Plocharski M, Østergaard LR. Extraction of sulcal medial surface and classification of Alzheimer's disease using sulcal features. *Comput Methods Prog Biomed*. 2016;133:35–44.
- Ratcliff R. Modeling aging effects on two-choice tasks: response signal and response time data. *Psychol Aging*. 2008;23(4):900–916.
- Roe JM, Vidal-Piñeiro D, Sørensen Ø, Brandmaier AM, Düzel S, Gonzalez HA, Kievit RA, Knights E, Kühn S, Lindenberger U, et al. Asymmetric thinning of the cerebral cortex across the adult lifespan is accelerated in Alzheimer's disease. *Nat Commun*. 2021;12(1):721.
- Rolls ET, Mills WPC. Computations in the deep vs superficial layers of the cerebral cortex. *Neurobiol Learn Mem*. 2017;145:205–221.
- Romito-DiGiacomo RR, Menegay H, Cicero SA, Herrup K. Effects of Alzheimer's disease on different cortical layers: the role of intrinsic differences in Abeta susceptibility. *J Neurosci*. 2007;27(32):8496–8504.
- Ruetten PPR, Gillard JH, Graves MJ. Introduction to quantitative susceptibility mapping and susceptibility weighted imaging. *Br J Radiol*. 2019;92(1101):20181016.
- Sacchi L, Contarino VE, Siggillino S, Carandini T, Fumagalli GG, Pietroboni AM, Arcaro M, Fenoglio C, Orunesu E, Castellani M, et al. Banks of the superior temporal sulcus in Alzheimer's disease: a pilot quantitative susceptibility mapping study. *J Alzheimers Dis*. 2023;93(3):1125–1134.
- Shin HG, Lee J, Yun YH, Yoo SH, Jang J, Oh SH, Nam Y, Jung S, Kim S, Fukunaga M, et al. In-vivo histology of iron and myelin in the brain using magnetic susceptibility source separation in MRI. *NeuroImage*. 2020;240:118371.
- Shin H-G, Lee J, Yun YH, Yoo SH, Jang J, Oh S-H, Nam Y, Jung S, Kim S, Fukunaga M, et al. χ -Separation: magnetic susceptibility source separation toward iron and myelin mapping in the brain. *NeuroImage*. 2021;240:118371.
- Smith MA, Harris PLR, Sayre LM, Perry G. Iron accumulation in Alzheimer disease is a source of redox-generated free radicals. *Proc Natl Acad Sci U S A*. 1997;94(18):9866–9868.
- Smith SM, Jenkinson M, Woolrich MW, Beckmann CF, Behrens TEJ, Johansen-Berg H, Bannister PR, De Luca M, Drobnjak I, Flitney DE, et al. Advances in functional and structural MR image analysis and implementation as FSL. *NeuroImage*. 2004;23:S208–S219.
- Spotorno N, Acosta-Cabronero J, Stomrud E, Lampinen B, Strandberg OT, van Westen D, Hansson O. Relationship between cortical iron and tau aggregation in Alzheimer's disease. *Brain*. 2020;143(5):1341–1349.
- Sui YV, Masurkar AV, Rusinek H, Reisberg B, Lazar M. Cortical myelin profile variations in healthy aging brain: a T1w/T2w ratio study. *NeuroImage*. 2022;119743:119743.
- Taege Y, Hagemeyer J, Bergsland N, Dwyer MG, Weinstock-Guttman B, Zivadinov R, Schweser F. Assessment of mesoscopic properties of deep gray matter iron through a model-based simultaneous analysis of magnetic susceptibility and R(2)* - a pilot study in patients with multiple sclerosis and normal controls. *NeuroImage*. 2019;186:308–320.
- Tournier J, Smith R, Raffelt D, Tabbara R, Dhollander T, Pietsch M, Christiaens D, Jeurissen B, Yeh C-H, Connolly A. MRtrix3: a fast, flexible and open software framework for medical image processing and visualisation. *NeuroImage*. 2019;202:116137.
- van Bergen JM, Li X, Hua J, Schreiner SJ, Steininger SC, Quevenno FC, Wyss M, Gietl AF, Treyer V, Leh SE, et al. Colocalization of cerebral iron with amyloid beta in mild cognitive impairment. *Sci Rep*. 2016;6(1):35514.
- Veale T, Malone IB, Poole T, Parker TD, Slattery CF, Paterson RW, Foulkes AJM, Thomas DL, Schott JM, Zhang H, et al. Loss and dispersion of superficial white matter in Alzheimer's disease: a diffusion MRI study. *Brain Commun*. 2021;3(4):fcab272.
- Vogt O, Vogt C. Zur anatomischen Gliederung des cortex cerebri. *J Psychol Neurol*. 1903;2:160–180.
- Waehnert MD, Dinse J, Weiss M, Streicher MN, Waehnert P, Geyer S, Turner R, Bazin PL. Anatomically motivated modeling of cortical laminae. *NeuroImage*. 2014;93:210–220.
- Waehnert MD, Dinse J, Schäfer A, Geyer S, Bazin P-L, Turner R, Tardif CL. A subject-specific framework for in vivo myeloarchitectonic analysis using high resolution quantitative MRI. *NeuroImage*. 2016;125:94–107.
- Walhovd KB, Fjell AM, Dale AM, McEvoy LK, Brewer J, Karow DS, Salmon DP, Fennema-Notestine C. Multi-modal imaging predicts memory performance in normal aging and cognitive decline. *Neurobiol Aging*. 2010;31(7):1107–1121.

- Ward RJ, Zucca FA, Duyn JH, Crichton RR, Zecca L. The role of iron in brain ageing and neurodegenerative disorders. *Lancet Neurol*. 2014;13(10):1045–1060.
- Wechsler D. WAIS--III: Wechsler adult intelligence scale. In: *Administration and scoring manual*. 3rd ed. San Antonio, TX: The Psychological Corporation; 1997.
- Yan F, He N, Lin H, Li R. Iron deposition quantification: applications in the brain and liver. *J Magn Reson Imaging*. 2018;48(2):301–317.
- Yang A, Du L, Gao W, Liu B, Chen Y, Wang Y, Liu X, Lv K, Zhang W, Xia H, et al. Associations of cortical iron accumulation with cognition and cerebral atrophy in Alzheimer's disease. *Quant Imaging Med Surg*. 2022;12(9):4570–4586.
- Zecca L, Youdim MBH, Riederer P, Connor JR, Crichton RR. Iron, brain ageing and neurodegenerative disorders. *Nat Rev Neurosci*. 2004;5(11):863–873.
- Zhao Z, Zhang L, Wen Q, Luo W, Zheng W, Liu T, Zhang Y, Zhu K, Wu D. The effect of beta-amyloid and tau protein aggregations on magnetic susceptibility of anterior hippocampal laminae in Alzheimer's diseases. *NeuroImage*. 2021;244:118584.
- Zhu WZ, Zhong WD, Wang W, Zhan CJ, Wang CY, Qi JP, Wang JZ, Lei T. Quantitative MR phase-corrected imaging to investigate increased brain iron deposition of patients with Alzheimer disease. *Radiology*. 2009;253(2):497–504.